MHN-SLAM FOR PLANETARY LANDING

Corey Marcus,* Renato Zanetti†

Simultaneous Localization and Mapping (SLAM) has a strong potential for use in autonomous landing scenarios. It could be used in real-time to identify hazards and potential landing sites which were unknown *a priori* during the terminal descent phase. Landers using SLAM could visit regions which are too hazardous for ones employing existing technologies. Previous relative navigation work between two on-orbit spacecraft showed that using the Modified-Half-Normal (MHN) distribution to represent mapping uncertainty in SLAM provides performance improvements over using the Gaussian distribution. In this work, we show that SLAM with the MHN distribution also provides effective tracking and mapping during a simulated autonomous landing scenario.

INTRODUCTION

Many future robotic missions across the solar system will include a landing phase. They will target scientifically interesting sites which are often filled with environmental hazards such as rocks and craters. Light time delays mandate an autonomous onboard landing system to detect and avoid these hazards. Traditionally, missions to Mars have relied on hazard maps generated before flight from orbital imagery.[1] Techniques such as Terrain Relative Navigation localize the lander with respect to these *a priori* hazard maps.

Future landers may not have the luxury of *a priori* hazard maps due to cost constraints, low orbital visibility, or dynamic terrain. Recent missions to the Moon[2] and Mars[3] have autonomously identified hazards during descent using cameras. Future missions may be motivated to go farther and use their cameras to generate a map of the terrain during descent which can be searched for safe and scientifically interesting landing sites. A class of algorithms known as Simultaneous Localization and Mapping (SLAM) can produce such maps and localize the lander with respect to them.

Previous work has developed a monocular SLAM system utilizing the Modified Half Normal (MHN) distribution.[4] The MHN distribution is a three parameter distribution for positive random variables. A nonlinear estimator was derived leveraging the MHN distribution and was shown to provide more accurate Bayesian updates to an uncertain depth state than an Extended Kalman Filter (EKF). A SLAM system employing this estimator demonstrated superior performance to one based on an EKF when employed in a spacecraft proximity operations scenario. In this work, we will demonstrate that the monocular MHN-SLAM system can also provide tracking and mapping in a simulated landing scenario.

*PhD Student, Aerospace Engineering and Engineering Mechanics, The University of Texas at Austin, cmarcus@utexas.edu.

†Assistant Professor, Aerospace Engineering and Engineering Mechanics, The University of Texas at Austin.

RELATED WORK

SLAM has a rich history dating back at least to Cheeseman et al. who proposed using an Extended Kalman Filter (EKF) to estimate the relative position and orientation between an observer and several landmarks in a 2D domain.[5] This work quickly evolved into well known EKF-SLAM algorithms which used visual features extracted from monocular camera images.[6] Many authors highlighted consistency and time complexity issues with EKF-SLAM methods which culminated in the seminal work by Strasdat et al.[7] which resulted in a shift from filtering algorithms to algorithms centered on nonlinear least squares optimization.

These optimization-based approaches often leverage a technique known as Bundle Adjustment where reprojection errors between feature correspondences are minimized by adjusting camera poses and feature locations.[8] Nonlinear least squares schemes can have their own issues with time-complexity and the inability to marginalize previous measurements into a prior.

Our previous work on Modified-Half-Normal SLAM (MHN-SLAM) sought to find a middle ground between the drawbacks of filter and nonlinear least squares methods.[4] We noted that many of the EKF-SLAM problems were induced by the linearization required for applying Bayes Rule and the possibility of non-physically realizable negative depths in some map representations. A nonlinear Bayesian estimator was derived for monocular camera measurements of a feature with a MHN prior on its depth. The MHN distribution had the added benefit of being strictly positive; eliminating the possibility of negative depth estimates. It was shown that MHN-SLAM provided notable performance improvements over a similar EKF based system in a proximity operations scenario using synthetic images of a target spacecraft. In this work we show that the MHN-SLAM system can also provide benefits for a planetary landing scenario.

SLAM and related algorithms have been applied to landing many times. Setterfield et al. present a loosely coupled terrain relative navigation (TRN) and mapping system.[9] TRN is performed with respect to an *a priori* known map using lidar scans. Pose estimates are found by optimizing a graph containing a combination of TRN and inertial measurements. The lidar scans also update the map but only the *a priori* version is used for TRN.

Givens and McMahon implement a square root information filter for SLAM in a planetary landing scenario.[10] Their system produces equivalent results to an EKF-SLAM system without explicit marginalization of old map features to maintain constant-time complexity. Unlike our system, they are able to formulate a tightly coupled filter for pose and map estimates. However; they continue to use the Gaussian distribution as opposed to our MHN.

Andert et al. showcase a visual SLAM system for lunar landing which includes a single lidar point measurement to resolve the scale ambiguity.[11] In addition to visual features, they detect crater rim ellipses which can be matched to a catalog for absolute navigation purposes. Mapping and tracking are performed as sequential sub-problems. Each is solved with a Levenberg-Marquardt optimization scheme to minimize reprojection error.

Another implementation by Nakath et al. has a SLAM module as one subsystem within a larger guidance, navigation, and control architecture.[12] Their implementation is tailored towards a satellite searching for landing sites while orbiting a small asteroid. The SLAM consists of a graph which is iteratively optimized with a g2o framework[13] wrapped around an EKF to estimate relative transformations between nodes.

In the atmospheric domain Yang et al. design a SLAM system for autonomous rotor-craft landing.[14] ORB-SLAM2[15] forms the basis for their SLAM system. ORB[16] features are extracted from monocular camera images and the SLAM estimates are produced with nonlinear least squares optimization. They apply a 2.5D grid map to the 3D points in order to search for suitable landing sites.

PRELIMINARIES

Camera Conventions

Every camera image establishes dual sets of coordinates: one in the form of a 3D spatial frame denoted as $\mathcal{C}$, and the other as a 2D image frame denoted as $\mathcal{I}$. This arrangement is illustrated in Figure 1.
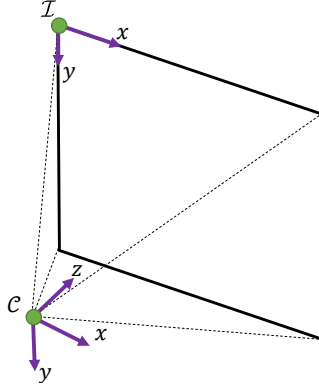

Figure 1: The coordinate frames used in this work. $\mathcal{C}$ defines the camera coordinate frame and has its origin at the camera aperture. The z axis is aligned with the camera's boresight. $\mathcal{I}$ is a 2D coordinate frame for the image. Its x and y coordinates increase towards the bottom-right corner.

We use a pinhole camera model in which a camera's intrinsic parameters are defined by its focal lengths f_x and f_y and the principal point coordinates σ_x and σ_y. These parameters are modeled in the camera calibration matrix K:

$$K = \begin{bmatrix} f_x & 0 & \sigma_x \\ 0 & f_y & \sigma_y \\ 0 & 0 & 1 \end{bmatrix}. \tag{1}$$

A feature, r, in $\mathcal{C}$, $r^{\mathcal{C}}$ can be transformed to $\mathcal{I}$ using the nonlinear mapping $p^{\mathcal{I}} = \pi(r^{\mathcal{C}})$,

$$\begin{bmatrix} x' \\ y' \\ z' \end{bmatrix} = Kr^{\mathcal{C}} \rightarrow p^{\mathcal{I}} = \pi(r^{\mathcal{C}}) = \begin{bmatrix} x'/z' \\ y'/z' \end{bmatrix}. \tag{2}$$

Multiplicative Extended Kalman Filter

Upon processing the initial image through our system, we establish the SLAM map frame, $\mathcal{C}_1$, in which pose estimates are found. The task of attitude estimation poses challenges due to the absence of a non-singular three-dimensional representation for rotations. Quaternions provide an alternative approach that avoids singularity issues, albeit by introducing an extra parameter and adhering to a unit norm restriction.

3

Furthermore, complexities arise from the fact that rotations are combined multiplicatively rather than additively. To tackle these challenges, the Multiplicative Extended Kalman Filter (MEKF)[17] was developed. It accomplishes this by estimating an unconstrained three-vector parameterization denoted as $\hat{a}$, representing the rotation between the true attitude and a reference attitude in the standard EKF update stage. Singularities are circumvented by assuming that the attitude error remains small. Following the Kalman update, $\hat{a}$ is utilized to update the reference attitude, and then $\hat{a}$ is reset to zero prior to the subsequent propagation phase.

The full state at the ith time-step carried by our MEKF is

$$
x_i = \begin{bmatrix} t_{\mathcal{C}_i}^{\mathcal{C}_1} \\ a_i \\ v_{\mathcal{C}_i}^{\mathcal{C}_1} \\ \omega_{\mathcal{C}_i/\mathcal{C}_1}^{\mathcal{C}_i} \end{bmatrix}.
\tag{3}
$$

We represent the position of the camera with respect to and expressed in the map frame as $t_{\mathcal{C}_i}^{\mathcal{C}_1}$. To model the error quaternion we use twice its vector component and denote the variable $a_i = 2(\delta q_{\hat{\mathcal{C}}_i}^{\mathcal{C}_i})_v$. Outside of our state estimate, we track a nominal quaternion from the map frame to the estimated camera frame, $q_{\mathcal{C}_1}^{\hat{\mathcal{C}}_i}$. The true quaternion from map to camera frame is defined as $q_{\mathcal{C}_1}^{\mathcal{C}_i} = \delta q_{\hat{\mathcal{C}}_i}^{\mathcal{C}_i} \otimes q_{\mathcal{C}_1}^{\hat{\mathcal{C}}_i}$ where $\otimes$ is the Shuster quaternion multiplication.[18] Velocity of the camera with respect to and expressed in the map frame is $v_{\mathcal{C}_i}^{\mathcal{C}_1}$. Finally, we term the angular velocity of the camera with respect to the map frame in the camera frame as $\omega_{\mathcal{C}_i/\mathcal{C}_1}^{\mathcal{C}_i}$. Details on our pose estimation scheme are outlined in our previous work.[4] In this implementation our MEKF uses a constant velocity and angular rate physics model for the time-propagation stage.

MHN Distribution

We heavily leverage the modified half normal (MHN) probability distribution in this work. It is a three parameter continuous distribution for strictly positive random variables.[19] Its three parameters are α, β, and γ. They have allowable values of $\alpha > 0$, $\beta > 0$, and $\gamma \in \mathbb{R}$.

$$
p_{\text{MHN}}(x|\alpha,\beta,\gamma) = \frac{2\beta^{\alpha/2}x^{\alpha-1}e^{-\beta x^2+\gamma x}}{\Psi[\frac{\alpha}{2},\frac{\gamma}{\beta}]} \ \forall \, x > 0
\tag{4}
$$

$\Psi[\frac{\alpha}{2}, z]$ is shorthand for a specific case of the Fox-Wright Psi function.[20,21]

$$
\Psi[\frac{\alpha}{2}, z] = {}_1\Psi_1 \begin{bmatrix} (\alpha/2, 1/2); \\ (1, 0) \end{bmatrix} z
\tag{5}
$$

Expressions for the mean and variance of an MHN distributed random variable x are shown below

$$
\mathrm{E}[x] = \frac{\Psi[\frac{\alpha+1}{2}, \frac{\gamma}{\sqrt{\beta}}]}{\sqrt{\beta}\Psi[\frac{\alpha}{2}, \frac{\gamma}{\sqrt{\beta}}]}
\tag{6}
$$

$$
\mathrm{E}[(x - \mathrm{E}[x])^2] = \frac{\alpha}{2\beta} + \mathrm{E}[x]\left(\frac{\gamma}{2\beta} - \mathrm{E}[x]\right).
\tag{7}
$$

MHN UPDATE

The MHN update was originally derived in our previous work.[4] We present the results of the derivation here. Figure 2 outlines our measurement model and the various coordinate systems used in this work. We use F to represent a feature imaged twice from different vantage points. Each camera image defines two coordinate systems, and we have an estimate of the relative pose between the camera images.
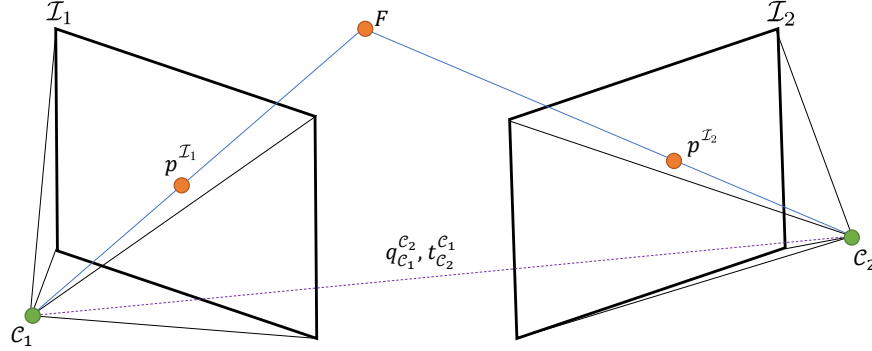

Figure 2: The physical setup for a stereo comparison. F is observed from two vantage points. The two images define coordinate systems $\mathcal{C}_1$ and $\mathcal{C}_2$. We locate the point in each image $\mathcal{I}_1$ and $\mathcal{I}_2$. Its pixel coordinates are defined as $p^{\mathcal{I}_1}$ and $p^{\mathcal{I}_2}$. Relative pose between the vantage points is represented with the position $t^{\mathcal{C}_1}_{\mathcal{C}_2}$ and quaternion $q^{\mathcal{C}_2}_{\mathcal{C}_1}$.

Our measurement is pixel disparity

$$\lambda = \sqrt{\sum_{j=x,\,y} \left(p^{\mathcal{I}_2}_j - p^{\mathcal{I}_1}_j \right)^2}. \tag{8}$$

Our previous work outlines how uncertainty in the depth of F with respect to $\mathcal{C}_1$, d, can be represented with an MHN distribution.[4] The parameters of the distribution are updated with each measurement λ according to Equations (9)-(11). A recursive, nonlinear, Bayesian estimator was formulated using these update laws.

$$\hat{\alpha} = \alpha + 2 \tag{9}$$

$$\hat{\beta} = \beta + \beta' \lambda^2 \tag{10}$$

$$\hat{\gamma} = \gamma + \gamma' \lambda. \tag{11}$$

The parameters β' and γ' can be found numerically by solving the following nonlinear system of equations.

$$2\Sigma_\Gamma + \mu_x^2 + \mu_y^2 = \frac{1}{\beta'} + \frac{\gamma'}{2\beta'} \frac{\Psi[\frac{3}{2}, \frac{\gamma'}{\sqrt{\beta'}}]}{\sqrt{\beta'}\Psi[\frac{2}{2}, \frac{\gamma'}{\sqrt{\beta'}}]} \tag{12}$$

$$\sqrt{\frac{\Sigma_\Gamma \pi}{2}} L_{1/2} \left(-\frac{\mu_x^2 + \mu_y^2}{2\Sigma_\Gamma} \right) = \frac{\Psi[\frac{3}{2}, \frac{\gamma'}{\sqrt{\beta'}}]}{\sqrt{\beta'}\Psi[\frac{2}{2}, \frac{\gamma'}{\sqrt{\beta'}}]} \tag{13}$$

Here, $L_{1/2}(\cdot)$ is the Laguerre Polynomial of order $1/2$. The parameters μ_x, μ_y, and Σ_Γ are scalar constants related to the predicted value of $p^{\mathcal{I}_2}$ given the MHN prior on d. Precise details are available in our previous work.

Filter Initialization

We use new measurements to update our estimate of feature depth. Filter initialization requires us to choose the initial MHN parameters, $(\alpha_0, \beta_0, \gamma_0)$. We will choose these parameters such to satisfy a desired initial mean, μ, and variance, Σ. This system is under-constrained and has multiple solutions. Choosing $\alpha_0 = 1$ reduces the number of remaining solutions to one. To find the other two parameters we use a Levenberg-Marquardt optimization routine to choose β_0 and γ_0 such that the mean and variance of our initial distribution match μ and Σ.

SLAM

We have developed a monocular SLAM system utilizing our MHN filter. SLAM is performed in a simulation of spacecraft descent onto a planetary surface while operating a monocular camera. We assume perfect frame to frame feature tracking is available through some algorithm such as ORB.[16] Using these camera images, the system estimates terrain structure, terrain relative pose, velocity, and angular rates.

System Initialization

Figure 3 provides an overview of our SLAM system. The system can be roughly divided into a tracking and mapping module. A tracking estimate is provided for each new image which the system acquires using features which are identified in the image as well as the system's map estimate. Afterwards, the mapping module uses the tracking estimate to update the map.
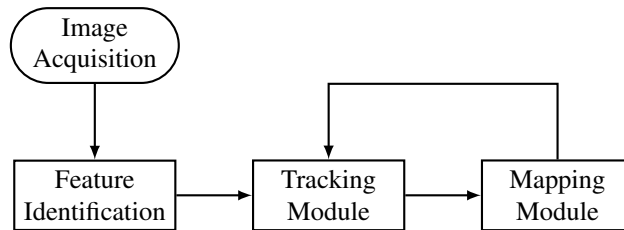

Figure 3: Our SLAM system. We assume that accurate feature identification has been performed by some external algorithm. Tracking estimates are found by comparing new images to the existing map. The map is further refined with these estimates.

SLAM begins when the first image arrives. This image forms the basis of the SLAM coordinate frame, $\mathcal{C}_1$, according to the conventions in Figure 1. We assume that a feature tracking algorithm has provided a set of features which correspond to the terrain. We also assume availability of ground plane estimate.

All tracking is performed with respect to the SLAM coordinate frame defined by the first camera image. This means the initial tracking estimates are for zero rotation and zero translation. Each feature in $\mathcal{C}_1$ forms a ray which we intersect with the ground plane estimate. We corrupt the depth of this intersection point

with Gaussian noise and use the corrupted point as our initial depth estimate. MHN depth estimates are initialized as described previously.

Tracking

Tracking is performed with an MEKF. We generate measurements of relative position, $r_{\mathcal{C}_1 \to \mathcal{C}_i}^{\mathcal{C}_i}$, and the error quaternion parameterization, a. This is done by projecting the estimated map into the predicted camera frame and choosing $r_{\mathcal{C}_1 \to \mathcal{C}_2}^{\mathcal{C}_i}$ and a to minimize reprojection error between all matched features.

These measurements are fused with the prior to produce an estimate of camera pose, velocity, and body rates using the MEKF formulation outlined previously.

Mapping

The mapping system is used to estimate the depth, d, or z component of each feature in $\mathcal{C}_1$. We assume that a feature tracking algorithm identifies map features in each new camera image. To compare performance we may either represent depth estimates with a Gaussian or an MHN distribution. Gaussian depth estimates are updated with a simple EKF. We use Equations (9-11) to update MHN depth estimates. Many filters include a prediction phase where the estimate is propagated through uncertain dynamics in time. Since terrain is typically static during a terminal descent we do not use a prediction phase.

RESULTS

We simulate a spacecraft approaching a lunar terrain containing a variety of boulders and craters. We assume trackable visual features are randomly distributed on the surface of these environmental features and that some feature extraction and matching algorithm has provided their locations in each image to the SLAM system. The terrain is shown in Figure 4. The simulated visual features are shown in Figure 5.

Our spacecrafts approach trajectory along with the simulated terrain is shown in Figure 6. The spacecraft is initially moving in a direction orthogonal to the terrain bearing for better depth observability. After several images a 90 degree turn is performed and the spacecraft moves towards the terrain.

Absolute scale is not observable in monocular SLAM. To accurately judge our system's performance we find an estimate of scale, $\hat{s}$, as the average ratio between the true and observed feature depths after each image is processed. We generate a combined metric of mapping and localization error by comparing the true and estimated map with respect to the camera frame after each image is processed. Each map point is transformed into the $\mathcal{C}_i$ frame using the SLAM estimated pose and post-process estimated scale.

$$\hat{F}^{\mathcal{C}_i} = \hat{q}_{\mathcal{C}_1}^{\mathcal{C}_i} \circ \hat{s} \left(\hat{F}^{\mathcal{C}_1} - \hat{t}_{\mathcal{C}_i}^{\mathcal{C}_1} \right) \tag{14}$$

Errors in the estimates $\hat{s}$, $\hat{q}_{\mathcal{C}_1}^{\mathcal{C}_i}$, $\hat{F}^{\mathcal{C}_1}$, and $\hat{t}_{\mathcal{C}_i}^{\mathcal{C}_1}$ contribute to errors in $\hat{F}^{\mathcal{C}_i}$.

We perform 100 run Monte Carlo for our SLAM system twice; once with MHN depth map updates and again with EKF map updates. For all instances and all map points we find the error in $\hat{F}^{\mathcal{C}_i}$. At each image, we find the RMS of this error. These RMS errors are averaged across Monte Carlo runs and the averages are plotted in Figure 7. We note that the average RMS error for the MHN system is significantly lower than the EKF system, indicating superior SLAM performance.

Figure 8 shows an example SLAM map created by an MHN system. The map's x and y axes represent the pixel coordinates at which the map feature is first observed. Color signifies estimated depth.
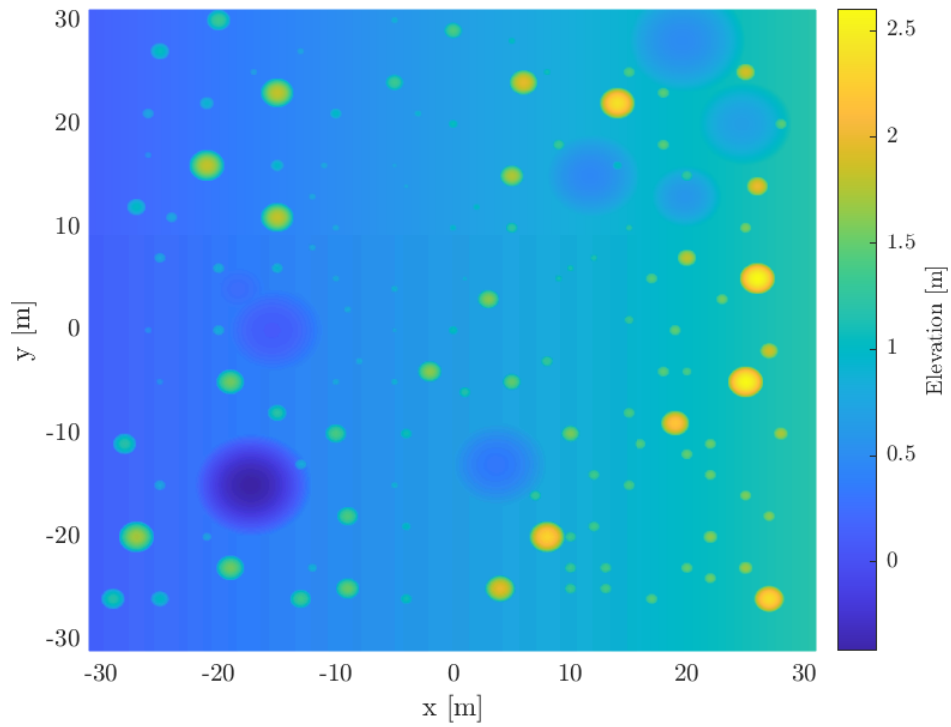
Figure 4: An elevation map of the simulated lunar terrain containing a collection of rocks and craters.

Figure 8 shows an example trajectory created by the MHN system in the terrain's coordinate frame. The system is generally able to capture the direction of camera motion but inertial drift errors quickly become significant. Future work is needed to address this drift so that the system may provide consistent localization estimates.
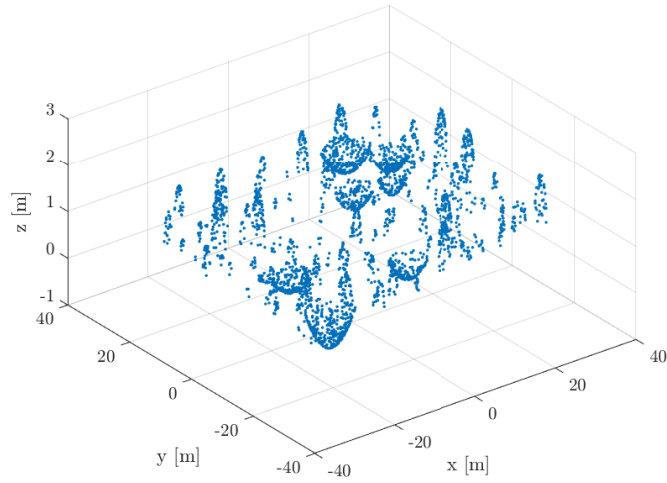
Figure 5: The point cloud of simulated visual features which are randomly and uniformly distributed across the rocks and craters of the lunar terrain.
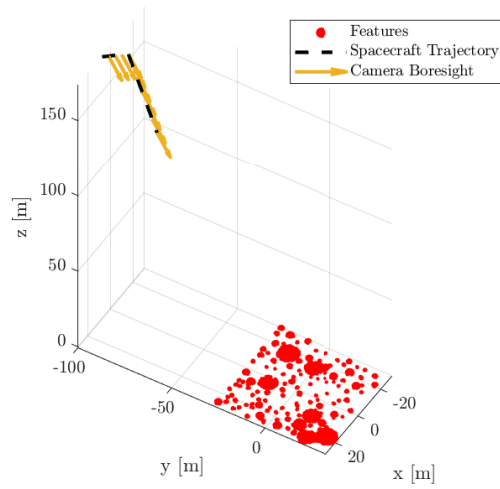

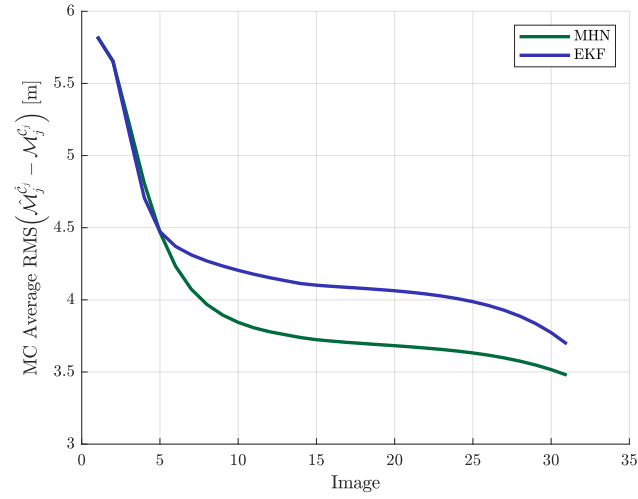**Figure 6**: The true vehicle trajectory and terrain features which it observes.

Figure 7: Average RMS mapping error across all Monte Carlo runs for each system configuration.
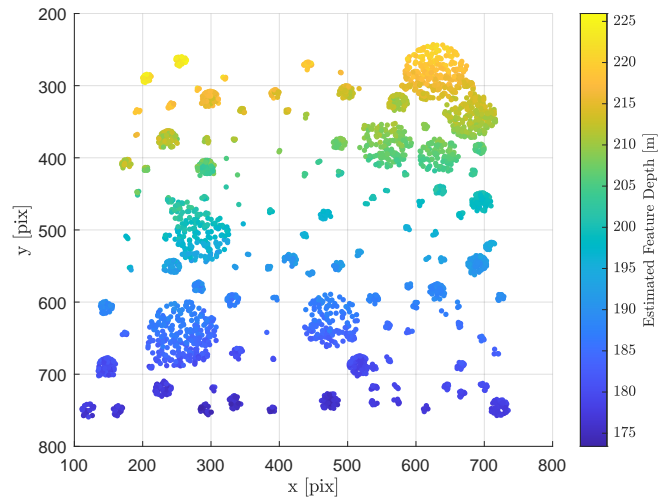

Figure 8: A representative estimated map created by the MHN-SLAM system during one Monte Carlo run.
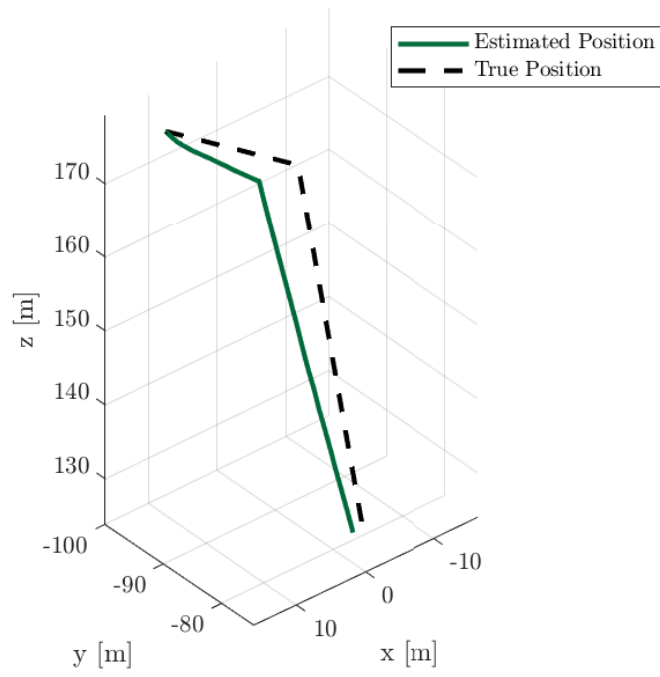
Figure 9: A representative estimated trajectory created by the MHN-SLAM system during one Monte Carlo run.

CONCLUSION

In this work we have presented preliminary results showing superior SLAM performance when using an MHN depth representation in a planetary landing scenario. Our simulation uses simulated images with perfect feature tracking while previous work has demonstrated efficacy with feature matching and artificial images of a target spacecraft in an on-orbit relative navigation scenario. Future work is needed to show MHN-SLAM can be effective in a planetary landing scenario when real images and feature tracking are incorporated.

ACKNOWLEDGMENTS

REFERENCES

[1] A. Nelessen, C. Sackier, I. Clark, P. Brugarolas, G. Villar, A. Chen, A. Stehura, R. Otero, E. Stilley, D. Way, K. Edquist, S. Mohan, C. Giovingo, and M. Lefland, "Mars 2020 Entry, Descent, and Landing System Overview," *2019 IEEE Aerospace Conference*, 2019, pp. 1–20.

[2] S. Li, X. Jiang, and T. Tao, "Guidance summary and assessment of the Chang'e-3 powered descent and landing," *Journal of Spacecraft and Rockets*, Vol. 53, No. 2, 2016, pp. 258–277.

[3] X. Huang, M. Li, X. Wang, J. Hu, Y. Zhao, M. Guo, C. Xu, W. Liu, Y. Wang, C. Hao, *et al.*, "The Tianwen-1 guidance, navigation, and control for Mars entry, descent, and landing," *Space: Science & Technology*, Vol. 2021, 2021.

[4] C. Marcus, R. Zanetti, and J. McCabe, "Improving Filter SLAM with the Modified-Half-Normal Distribution," *IEEE Transactions on Aerospace and Electronic Systems*, Vol. N/A, 2023, p. N/A. Under Review.

[5] P. Cheeseman, R. Smith, and M. Self, "A stochastic map for uncertain spatial relationships," *4th International Symposium on Robotic Research*, 1987, pp. 467–474.

[6] L. M. Paz, J. D. Tardós, and J. Neira, "Divide and conquer: EKF SLAM in $o(n)$," *IEEE Transactions on Robotics*, Vol. 24, No. 5, 2008, pp. 1107–1120.

[7] H. Strasdat, J. Montiel, and A. J. Davison, "Real-time monocular SLAM: Why filter?," *2010 IEEE International Conference on Robotics and Automation*, IEEE, 2010, pp. 2657–2664.

[8] B. Triggs, P. F. McLauchlan, R. I. Hartley, and A. W. Fitzgibbon, "Bundle adjustment—a modern synthesis," *International workshop on vision algorithms*, Springer, 1999, pp. 298–372.

[9] T. P. Setterfield, R. A. Hewitt, P.-T. Chen, A. T. Espinoza, N. Trawny, and A. Katake, "LiDAR-Inertial Based Navigation and Mapping for Precision Landing," *2021 IEEE Aerospace Conference (50100)*, 2021, pp. 1–19.

[10] M. W. Givens and J. W. McMahon, "Square-Root Extended Information Filter for Visual-Inertial Odometry for Planetary Landing," *Journal of Guidance, Control, and Dynamics*, Vol. 46, No. 2, 2023, pp. 231–245.

[11] F. Andert, N. Ammann, and B. Maass, "Lidar-aided camera feature tracking and visual slam for spacecraft low-orbit navigation and planetary landing," *Advances in Aerospace Guidance, Navigation and Control: Selected Papers of the Third CEAS Specialist Conference on Guidance, Navigation and Control held in Toulouse*, Springer, 2015, pp. 605–623.

[12] D. Nakath, J. Clemens, and C. Rachuy, "Active Asteroid-SLAM: Active Graph SLAM with Landing Site Discovery in a Deep Space Proximity Operations Scenario," *Journal of Intelligent & Robotic Systems*, Vol. 99, No. 2, 2020, pp. 303–333.

[13] G. Grisetti, R. Kümmerle, H. Strasdat, and K. Konolige, "g2o: A general framework for (hyper) graph optimization," *Proceedings of the IEEE International Conference on Robotics and Automation (ICRA)*, 2011, pp. 9–13.

[14] T. Yang, P. Li, H. Zhang, J. Li, and Z. Li, "Monocular vision SLAM-based UAV autonomous landing in emergencies and unknown environments," *Electronics*, Vol. 7, No. 5, 2018, p. 73.

[15] R. Mur-Artal and J. D. Tardós, "Orb-slam2: An open-source slam system for monocular, stereo, and rgb-d cameras," *IEEE Transactions on Robotics*, Vol. 33, No. 5, 2017, pp. 1255–1262.

[16] E. Rublee, V. Rabaud, K. Konolige, and G. Bradski, "ORB: An efficient alternative to SIFT or SURF," *2011 International conference on computer vision*, Ieee, 2011, pp. 2564–2571.

[17] F. L. Markley, "Multiplicative vs. additive filtering for spacecraft attitude determination," *Dynamics and Control of Systems and Structures in Space*, No. 467-474, 2004, p. 48.

[18] R. Zanetti, "Rotations, transformations, left quaternions, right quaternions?," *The Journal of the Astronautical Sciences*, Vol. 66, No. 3, 2019, pp. 361–381.

[19] J. Sun, M. Kong, and S. Pal, "The Modified-Half-Normal distribution: Properties and an efficient sampling scheme," *Communications in Statistics - Theory and Methods*, Vol. 0, No. 0, 2021, pp. 1–23.

[20] C. Fox, "The asymptotic expansion of generalized hypergeometric functions," *Proceedings of the London Mathematical Society*, Vol. 2, No. 1, 1928, pp. 389–400.

[21] E. M. Wright, "The asymptotic expansion of the generalized hypergeometric function," *Journal of the London Mathematical Society*, Vol. 1, No. 4, 1935, pp. 286–293.

[22] J. Sun, M. Kong, and S. Pal, "Supplementary Material For The Modified-Half-Normal distribution: Properties and an efficient sampling scheme," *Communications in Statistics - Theory and Methods*, 2021, pp. 1–41.